Science Advances

AAAS

advances.sciencemag.org/cgi/content/full/3/6/e1602051/DC1

Supplementary Materials for

Flexible and stretchable power sources for wearable electronics

Alla M. Zamarayeva, Aminy E. Ostfeld, Michael Wang, Jerica K. Duey, Igal Deckman, Balthazar P. Lechêne, Greg Davies, Daniel A. Steingart, Ana Claudia Arias

Published 16 June 2017, *Sci. Adv.* **3**, e1602051 (2017)
DOI: 10.1126/sciadv.1602051

This PDF file includes:

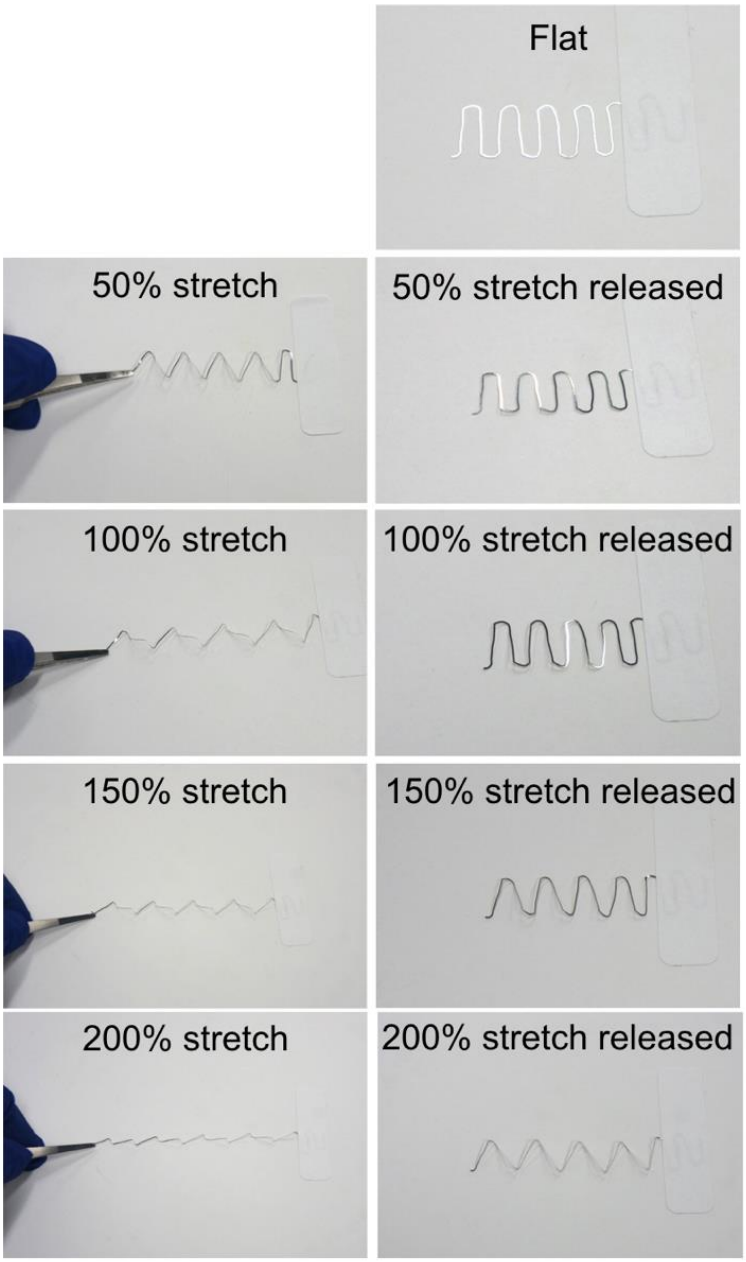

fig. S1. The optical images for the serpentine ribbon current collectors stretched to 50, 100, 150, and 200% before and after releasing the stretch.

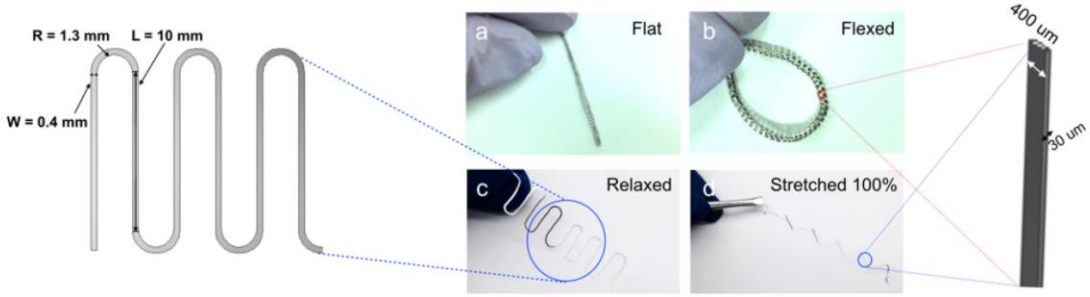

fig. S2. Dimensions and optical images of the helical band spring and serpentine ribbon current collectors. Optical images of the (**a** and **b**) helical band spring and (**c** and **d**) serpentine ribbon current collectors in a relaxed (a,c) and deformed (b,d) state. The schematics illustrate dimensions of the serpentine as well as thickness and width of the serpentine and helical band spring.

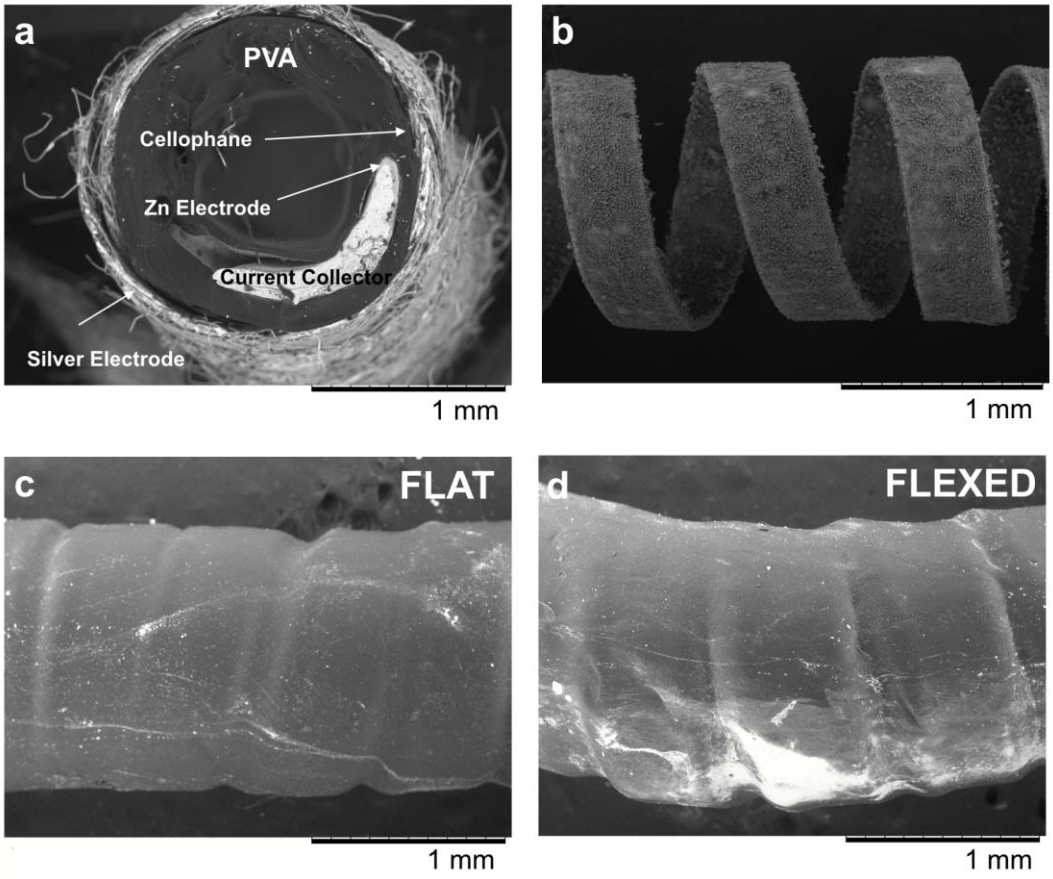

fig. S3. SEM images of the wire battery components. SEM image of the wire battery cross-section illustrating battery components (**a**). Helical spring current collector with electrodeposited Zn anode (**b**). Zn electrode coated with PVA polymer electrolyte in the flat configuration (**c**) and flexed to 1cm inner diameter (**d**).

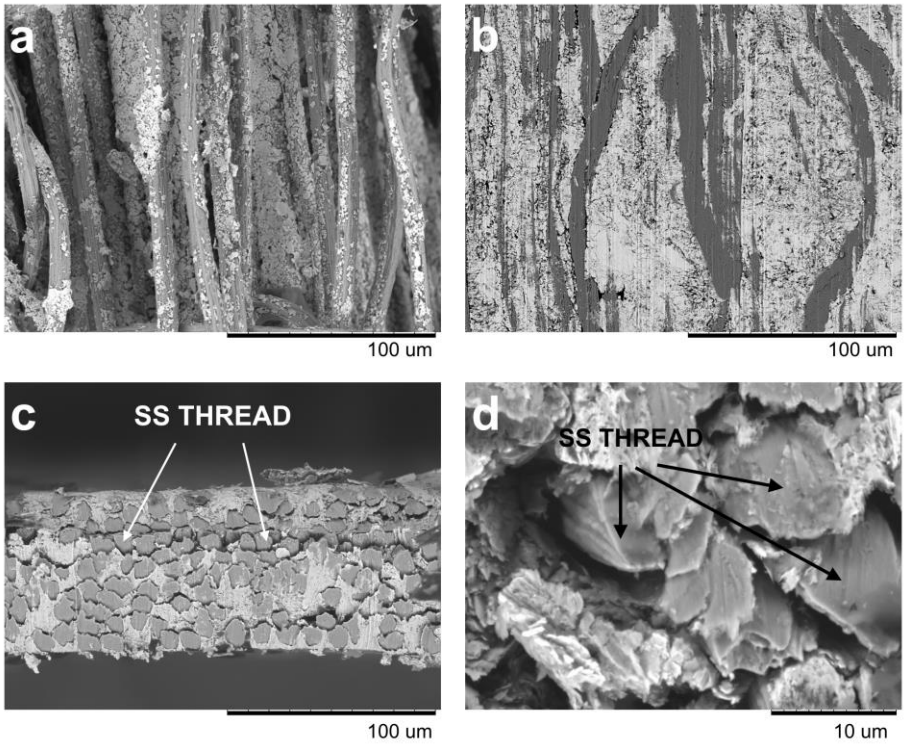

fig. S4. SEM characterization of the thread-embedded silver electrode. SEM micrograph of the top view (**a** and **b**) and cross section (**c** and **d**) of the silver electrode constructed by dip coating of the stainless steel (ss) thread into the silver nanoparticle ink before (a) and after (b-d) calendaring.

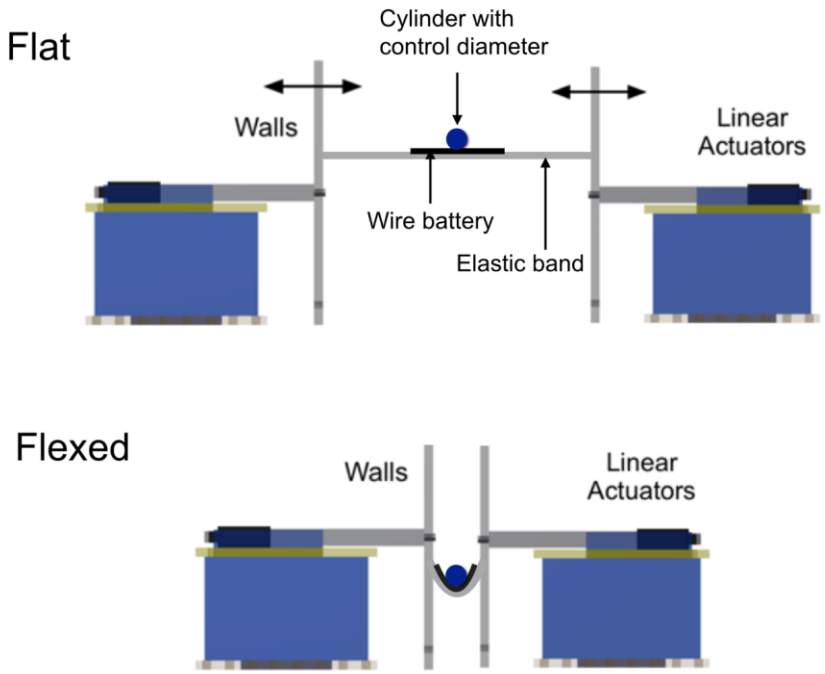

fig. S5. The schematic of the custom-made flexing apparatus. The battery is placed on the elastic band attached on both ends to the two linear actuators that control the flexing speed. Motion of linear actuators towards each other causes the elastic band to relax and bend.

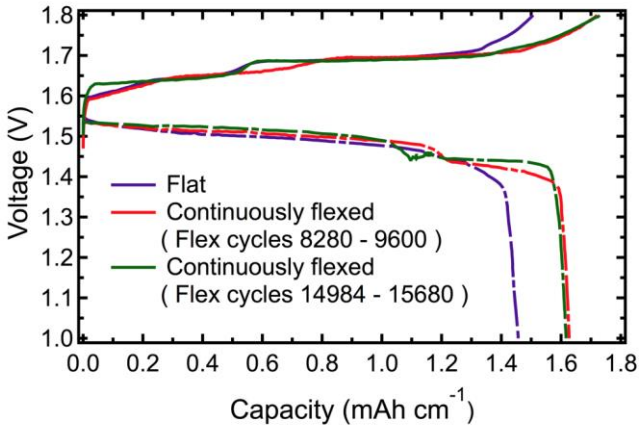

fig. S6. Charge-discharge curves of the wire battery operated under continuous flexing conditions. Galvanostatic charge-discharge curves for the 10th, 19th and 26th electrochemical cycle of the battery presented in Figure 2f. The charge-discharge curves for the 19th and 26th cycle were obtained while operating the battery under continuous flexing regime, when the curves for the 10th cycle were obtained while cycling the battery in a flat configuration. The overall capacity of the battery increases by over 10% as a result of flexing. The increase in capacity can be attributed to increase in the active surface area of the limiting Ag electrode and thus higher material utilization, as discussed in the Supplementary methods.

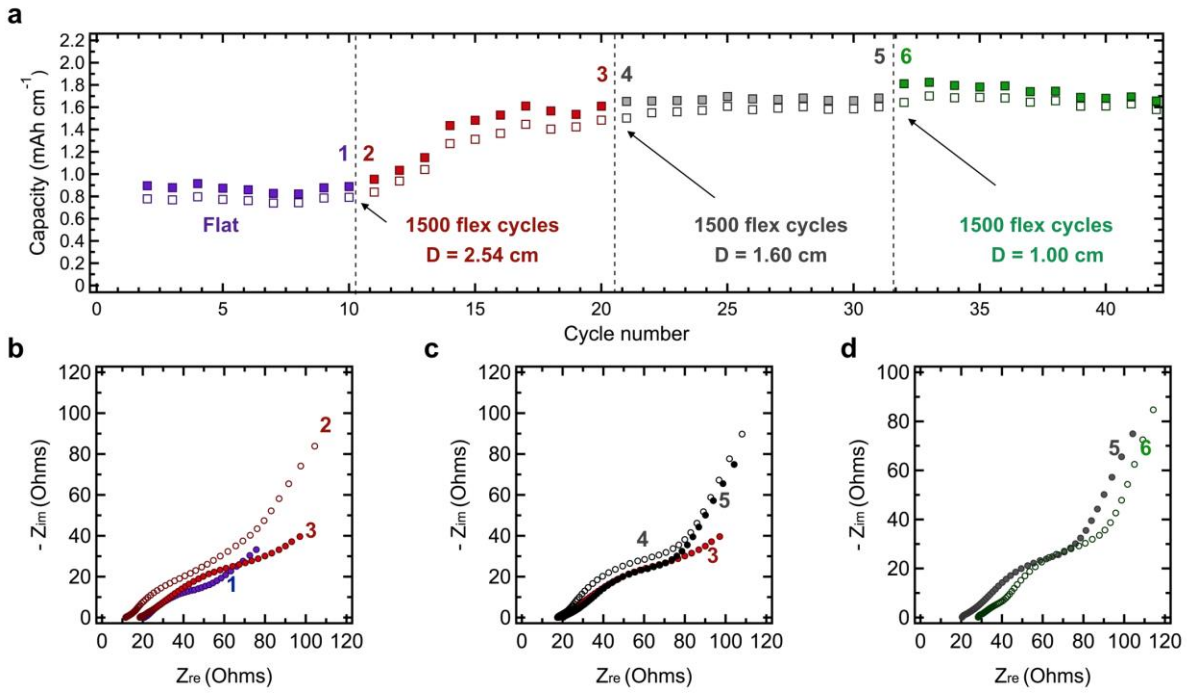

fig. S7. Electrochemical cycling performance of the wire battery that was periodically stopped and flexed 1500 times in between the electrochemical cycles. Nyquist plots of EIS measurements taken before and after flexing. (**a**) Cycling profile of the wire battery subjected to periodic flexing of 1500 flex cycles. The flexing diameter was decreased from 2.54 cm to 1.60 cm and to 1 cm after each set of flexing cycles. (**b** to **d**) The Nyquist plots of the EIS measurements taken before and after flexing to 2.54 cm, 1.60 cm and 1 cm respectively. EIS measurements were performed at frequencies ranging from 10^6 to 0.1 Hz at amplitude of 10 mV and were carried out while keeping the battery in a flat position.

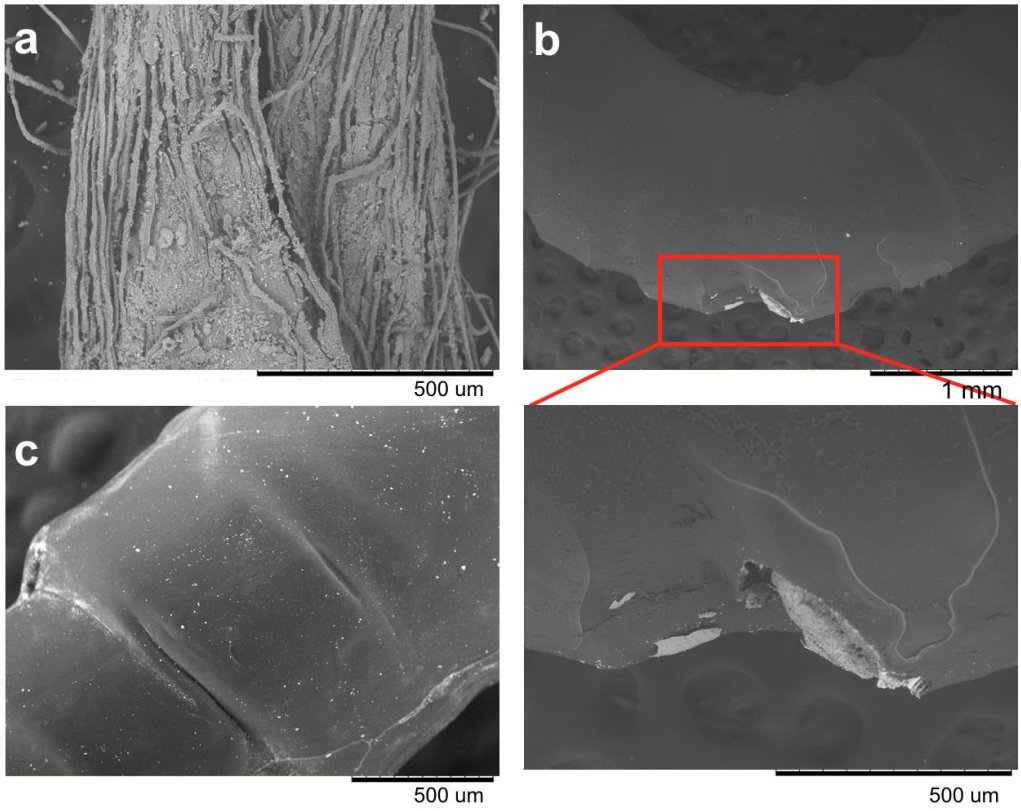

fig. S8. A postmortem analysis of the wire battery. SEM micrograph of cycled 180 times (in a charged state) silver electrode (**a**). Silver ink remains adhered to the thread after cycling. SEM images of the Copper-Zn-PVA composite after subjecting to 20 000 flexing cycles to the radius of 0.5 cm (**b** and **c**). Localized tear of the PVA polymer electrolyte caused by flexing (b). Plastic deformation of the polymer electrolyte layer in the regions in-between the coils, represented by wrinkling of the PVA (c). Since tears in the PVA layer lead to short circuits and consequent failure of the battery, the mechanical properties of the electrolyte-separator are the limiting factor to the mechanical performance of this system.

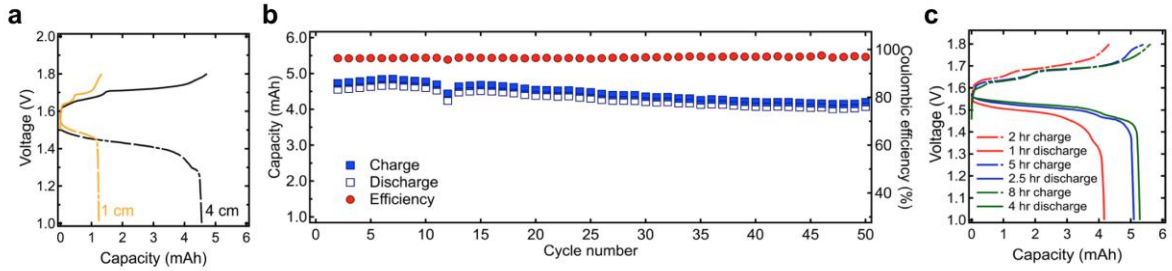

fig. S9. Performance characteristics of the 4-cm-long wire battery designed for integration with the solar module. (**a**) Galvanostatic charge-discharge curves of 1-cm (yellow) and 4-cm (black) silver-zinc wire battery operated at 0.25C charge and 0.5C discharge rates. (**b**) Capacity (mAh) and coulombic efficiency (%) of 4-cm battery cycled at 0.25C charge and 0.5C discharge rates between 1 V and 1.8 V. (**c**) Galvanostatic charge-discharge curves of 4-cm battery for charge rates 0.125C, 0.2C, 0.5C and discharge rates 0.25C, 0.4C, 1C respectively.

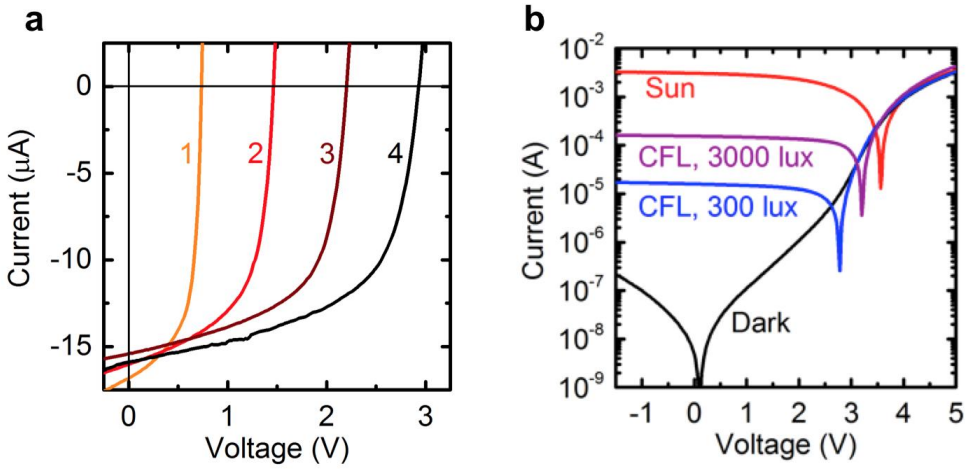

fig. S10. Performance characteristics of the OPV module designed for integration with the wire battery. (**a**) Current-voltage characteristics of 1-4 OPV cells in series, under CFL with illuminance of 300 lux. (**b**) Semilog plot of the current-voltage characteristics of 4-cell OPV modules under sunlight, CFL with illuminance of 300 and 300 lux, and in the dark.

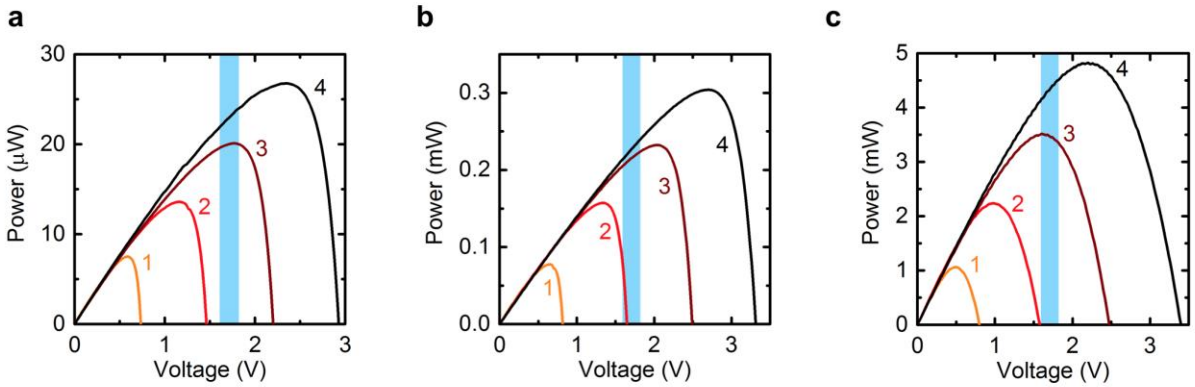

fig. S11. Power-voltage characteristics of the OPV module designed for integration with the wire battery. Power-voltage characteristics of 1-4 OPV cells in series, under CFL with illuminance of (**a**) 300 lux or (**b**) 3000 lux and (**c**) 1-sun. The blue shaded region represents the range of battery voltage during charging, 1.6-1.8V.

fig. S12. The schematic of the encapsulation of serpentine battery.

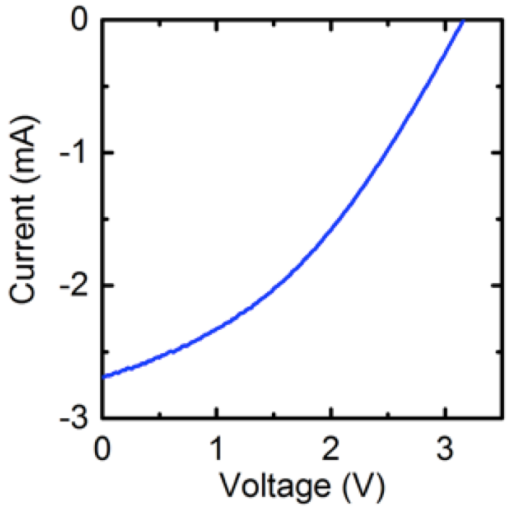

fig. S13. Current-voltage characteristic of the particular OPV module used to charge the wire battery under sunlight.

table S1. Performance parameters of single-OPV cells and four-cell modules under various lighting conditions.

Lighting		V_{OC} (V)	I_{SC} (mA)	FF	Module PCE (%)
CFL, 300 lux	Cell	0.72 ± 0.01	0.016 ± 0.001	0.60 ± 0.02	
	Module	2.7 ± 0.3	0.016 ± 0.0003	0.57 ± 0.06	6.6 ± 0.8
CFL, 3000 lux	Cell	0.81 ± 0.01	0.15 ± 0.01	0.62 ± 0.01	
	Module	3.1 ± 0.3	0.151 ± 0.006	0.61 ± 0.02	7.8 ± 0.8
Sunlight	Cell	0.87 ± 0.05	3.1 ± 0.3	0.45 ± 0.04	
	Module	3.6 ± 0.1	3.0 ± 0.1	0.42 ± 0.07	2.2 ± 0.4
LED, 300 lux	Module	2.4 ± 0.2	0.0082 ± 0.0001	0.54 ± 0.06	4.9 ± 0.5
LED, 3000 lux	Module	2.8 ± 0.3	0.075 ± 0.003	0.60 ± 0.02	5.9 ± 0.8

Supplementary Methods

EIS analysis of the processes occurring in the wire battery as a result of flexing

The specific capacity of as-fabricated flexible wire batteries based on spring current collector varies in the range 0.8 mAh cm^{-1} to 1.4 mAh cm^{-1} (caused by the manual assembly process of the limiting silver electrode) and increases after flexing up to 1.6 mAh cm^{-1}. To analyze processes occurring in the wire battery as a result of flexing that lead to the capacity increase, we performed electrochemical cycling, while periodically stopping and flexing the battery 1500 times in-between the electrochemical cycles. EIS measurements were carried out before and after flexing while keeping the battery in a flat position. The flexing diameter was decreased from 2.54 cm to 1.60 cm and finally to 1 cm after each set of flexing cycles. Figure S7a shows electrochemical cycling performance of the battery. The capacity first increases gradually from 0.8 mAh to 1.4 mAh following the first set of 1500 flexing cycles and then stabilizes with only minor increase immediately following each consecutive flexing cycle to a smaller radius. We speculate that increase in capacity after flexing was caused by increase in the active surface area between the limiting silver electrode and electrolyte. It is very likely to occur through formation of flexing-induced micro cracks in the thread-embedded silver electrode. Since electrolyte transport to the additional areas of the electrode does not occur instantaneously; the capacity increases gradually for the seven electrochemical cycles following the first set of flexing cycles. Minor increase in capacity immediately following second and third set of flexing cycles can be attributed to the formation of additional electro-active surfaces when battery is flexed to the smaller bending radii. To confirm our speculation we conducted analysis of the Nyquist plots from the EIS data.

The Nyquist plots consist of two depressed semicircles in the high to medium and medium to low frequency ranges and the sloping tail in the low frequency range. Inductive data obtained at high frequencies are not included in the plot, since they are irrelevant to the discussion and do not influence the rest of the impedance spectra (*40*).

The high frequency intercept with abscissa is attributed to the Ohmic resistance of the battery with the highest contribution from the electrolyte resistance (*40-42*). The two depressed semicircles represent kinetic impedance from both electrodes, dominated by the impedance of limiting silver electrode (*40-42*). The semicircles are depressed due to non-uniformity of the electrodes and thus varying capacitance and resistance contributions throughout the electrodes (*40*). The first semicircle was attributed to the charge transfer interfaces within the battery. The EIS response is dominated by the second semicircle, which was attributed to the Ag_2O surface coverage resistance (*40*). The low frequency spectrum of the battery impedance is influenced predominantly by solution diffusion Warburg process at Ag_2O cathode (*41*). Generally, increase in active surface area of an electrode results in the decrease of the kinetic impedance response due to increased area available for charge transfer (*43*). However, in zinc-silver system the response is overweighed by the contribution from Ag_2O coverage resistance. It is known that both Ag and Ag_2O are present in the electrode when the battery is discharged (*44-46*) and that Ag_2O is mechanically weaker then Ag (*46*). Therefore, when battery is flexed micro cracks are likely to occur at the areas of the electrode with high Ag_2O content, resulting in exposing more of the Ag_2O surface and increasing overall surface resistance of the electrode-electrolyte interface. If our speculations about the increase in capacity of the battery being caused by increase in the active surface area of silver electrode are correct, then increase in capacity would be reflected in the increase of the radius of the second semicircle of the Nyquist plot.

The Nyquist plots of the EIS measurements taken before and after flexing are presented in fig. S7, b to d. Curves 1 and 2 in fig. S7b correspond to Nyquist plots of the EIS measurements taken immediately before and after the first set of 1500 flexing cycles respectively. Curve 3 corresponds to the measurement taken after ten electrochemical cycles following the flexing. The increase in the radii of the second semicircle of the 2^{nd} and 3^{rd} curves corresponds to increase in capacity following the flexing and consecutive electrochemical cycling. Figures S7, c and d show Nyquist plots of the EIS measurements taken before and after second and third sets of flexing cycles. The second semicircle radii of these plots remain relatively constant. Thus, increase in capacity coincides closely with

the increase in the radii of the second semicircle in the EIS spectra, supporting our speculations that the increase in capacity of the battery is caused by increase in the active surface area of silver electrode. Therefore, as seen from both continuous and periodic flexing experiments, repetitive dynamic mechanical load did not seem to have a significant effect on the electrochemical performance of the wire battery. The capacity increase and insignificant increase in the impedance of the cell occurred as a result of flexing due to structural changes in the silver electrode.

Performance of the wire battery designed for integration with solar module

It is necessary to estimate the magnitude of the voltage drop to ensure that the battery of the chosen length is able to meet the energy requirements of the target system. Therefore, we compared galvanostatic charge-discharge curves of 1-cm and 4-cm batteries to estimate the magnitude of the potential drop associated with increased battery length. Figure S9a shows that the discharge plateau of the 4-cm battery exhibits ~0.049 V lower voltage values compared to the 1-cm battery, as estimated by midpoint voltage. On average, the observed potential drop was ~0.03 V and never exceeded ~0.05 V. The variations in voltage drop were caused by the manual assembly of the battery components and could be minimized by automating the assembly process. The 4-cm battery therefore provided the target discharge voltage of ~1.5 V despite increasing the length by 4 times. Since the increase in internal resistance of the device was small, the 4-cm battery was able to meet the energy requirement of >6 mWh.

Since the battery was sized for daily cycling, we investigated the cycling stability of the battery to ensure that it retains its capacity during cycling. The cycling profile of the battery is shown in figure S9b. The battery exhibited good performance, with an average capacity of 1.1 mAh, coulombic efficiency of ~96.5 %, and capacity retention of 88% after 50 electrochemical cycles. The minor decrease in capacity can be attributed to the migration of silver ions through the plastic seals towards the zinc electrode and subsequent poisoning of the electrode, coupled with factors associated with battery aging such as deterioration of the cellophane barrier and PVA separator and corrosion of the

current collectors. Therefore, the battery maintained the capacity set by the wearable accessory design parameters after 50 electrochemical cycles.

Because the rate of charge depends on the lighting conditions as well as the efficiency of the solar module, it is important to evaluate the performance of the 4-cm-long wire battery cycled at different charge-discharge rates in a range relevant to solar charging. The galvanostatic charge-discharge curves for the battery operated at different rates (0.125C, 0.2C, 0.5C charge and 0.25C, 0.4C, 1C discharge respectively) between 1 V and 1.8 V are shown in fig. S9c. Although the charge to discharge rate ratio will vary under real life conditions, the analysis of its effects on the battery performance is beyond the scope of the paper. Figure S6c shows that the range of charge voltage falls between 1.6 V and 1.8 V for all charge rates, which is within the window acceptable for the solar module. In addition, the battery retained capacity above 4 mAh over the range of discharge conditions.

Analysis of the ECSE of the solar cell–battery system

Although the battery voltage range is closer to the maximum power point of a 3-cell solar module than that of a 4-cell module, as seen in fig. S8, we chose to use the 4-cell module for battery charging because it provides greater total power and therefore a faster charging rate over that range. Additionally, since the battery voltage was below the maximum power point voltage of the 4-cell module, the module would be expected to produce nearly constant current during the entire charging period, particularly under the indoor lighting conditions when the fill factor is high. Furthermore, the open-circuit voltage of the 4-cell modules is well above the maximum battery voltage under all lighting conditions tested, leaving a sufficient margin for a blocking diode to be inserted between the OPV module and battery if needed in the future.

The efficiency of the solar charging system was evaluated under CFL illumination of 3000 lux and under sunlight. After each charging period with the solar module, the battery was discharged at a current of 4 mA, and the energy transferred in each step of the energy conversion and storage process was calculated in order to determine the energy

conversion and storage efficiency (ECSE), a figure of merit commonly used in solar supercapacitor charging systems (*51*). The total energy incident on the OPV module was 160 J for the 12-hour charging period under the CFL, and 2870 J for the 4-hour charging period in sunlight. The resulting energy output of the module, delivered to the battery, was determined by integrating the power output over the duration of the charging period and found to be 9.16 J and 36.0 J for the CFL and sunlight conditions. The average OPV module efficiency over the charging period was therefore 5.7% and 1.3%, respectively. The deviation between these efficiency values and the PCE in Supplementary table S1 is due in part to the fact that the OPV module is not operating exactly at its maximum power point during the charging period; instead, its voltage is set by the battery voltage. The efficiency under the 3000 lux CFL is in very good agreement with the power output at the battery voltage given in Supplementary fig. S11. Additionally, the values in table S1 are averages of several modules, and there was substantial variation in performance from one module to the next under sunlight due in large part to variation in series resistance. The particular module used to charge the battery in Figure 4f was at the low end of the performance range, with maximum 1-sun PCE of 1.6% and current-voltage characteristics given in Supplementary fig. S13. If an OPV module at the high end of the performance range had been used instead, the battery could be expected to charge nearly 40% faster. Thus, the variability of modules has a significant impact on the charging process. However, the improvement in efficiency for CFL illumination relative to sunlight is even greater than the variation in performance between individual modules.

When the battery was discharged at 4 mA following the CFL and sunlight charging periods, the energy extracted from the battery was 4.24 and 29.0 J, respectively, giving battery charge/discharge efficiencies of 46.3% and 80.6%. While the battery exhibits a high coulombic efficiency of 96.5%, the battery efficiency defined in terms of energy is lower because it includes the losses due to the potential difference of ~0.2V between charging and discharging. In addition, lower efficiencies are obtained if the battery is not operated at an optimum ratio of charge rate to discharge rate. Charge-discharge profile plays an important role in the efficiency of silver-zinc batteries, due to changes in the morphology of silver electrode with each electrochemical cycle. Slow charging rates,

such as the ~C/40 rate of charging with the OPV module under CFL lighting, have been shown to result in formation of larger size silver oxide particles (*37*). This leads to less efficient material access on discharge due to ionic transport limitations. Charging the battery under the sunlight conditions resulted in higher charging rate (~C/4) and, thus, formation of smaller size silver oxide particles, which could be more readily reduced on the consecutive discharge. Therefore, the obtained battery efficiency results are in good agreement with previous reports on the cycling of similar silver-zinc batteries (*37*).

Finally, the ECSE was calculated as the ratio of the energy extracted from the battery during discharging to the energy incident on the OPV module during charging. The OPV module efficiency and battery efficiency exhibited opposing trends with respect to light intensity: the OPV module efficiency was 4.4 times lower under sunlight than under the CFL, while the battery efficiency was 1.7 times higher. The ECSE, which is the product of these two efficiencies, was therefore 2.7 times higher under the CFL, 2.7% vs. 1.0%. Since the OPV module was the limiting factor in the 1-sun ECSE, improving the OPV module performance under sunlight should be the most effective way of improving the 1-sun ECSE. This could be accomplished by designing the module geometry to minimize series resistance, for example by using cells with a smaller aspect, as well as employing a more conductive transparent electrode. The low-light ECSE could be improved by using a smaller battery, so that the same OPV module current would equate to a larger C-rate, and therefore more optimal silver electrode morphology. However, reducing the battery capacity would limit the amount of solar energy that can be stored and the type and duration of loads that can be powered. Instead, optimizing the battery design for high efficiency at low charging rates could enable high low-light performance without sacrificing energy storage capacity.